Three-Dimensional Imaging and Reconstructions of Objects Under Rainy Conditions Using the Generation and Propagation of Coherent Structured Signal

Bingquan Chen, Peng Shi, Hongsheng Li, Hongxiu Gao, Ruirong Wang, Peng Gao, Xufei Wu, and Jun Yue

***Abstract*—This investigation is aiming at the development of a method for in-situ 3D imaging and reconstructions of objects in the rain. The proposed method is based on the use of monochromatic sinusoidal fringe pattern generated by the designed optical system, the polarization technique, and the Fourier-transform-based algorithm of reconstruction. Based on the theoretical analyses and experimental results, it shows that the generated laser-beam-based signal keeps being coherent until reaching the observed object. The coherence of the projected sinusoidal signal is the key feature of the proposed method and ensures the accuracy of measurement and reconstruction of objects under rainy conditions. Moreover, the effects resulted from the spectral absorption and multiple scattering on the propagation of the projected sinusoidal fringe pattern in the rain can be removed using the polarization technique. The developed method is capable of obtaining accurate 3D reconstructions of the objects under rainy conditions together with background illumination, the multiply-scattered light, the vibration from environmental influences including the wind, and the inhomogeneous medium of rain. The application of this method does not suffer the limitation of focusing, precise synchronization, and the speed of measurement that might be a problem for the time-of-flight technique and digital-light-processing-based profilometry.**

***Index Terms*—3D measurement, propagation, polarization, rain, random medium, reconstruction.**

I. Introduction

THE methods and technologies for non-contact and high-resolution shape measurement of three-dimensional (3D) objects have been attracting scientists and technologists during last few decades [1], [2]. Generally speaking, the existing approaches of 3D surface measurement are considered as belonging to the following categories, i.e. techniques based on passive stereo vision, active stereo vision, structured light, and time-of-flight (TOF) [3]. Even the passive technique, such as the stereo-vision approach, is relatively simple and has no need for active illumination on the object being observed, the development of accurate method and efficient algorithm for completing stereo matching on two images is still being a challenging issue [4], [5]. As far as the active method is concerned, there are two major methods. One active method is the TOF-based approach using an active emitter to modulate the light in time domain and an optical sensor to detect the signal scattered back by the object being observed for retrieving the depth information by calculating the time delay from the signal leaves the emitter and the signal returns to the detecting sensor, while obtaining high-depth-resolution measurement might be difficult because of the limit of measuring technique due to the high speed of light. The other active method is the approach using structured light, while the measuring process and reconstruction algorithm depend on the codification methods of the project structured patterns. The popular encoding methods include binary coding [6], sinusoidal phase encoding [7], [8], binary defocusing [9], [10], triangular phase-shifting method [11], and color coded structured patterns [12], [13]. Those encoding methods are mostly based on the computer-controlled DMD-chip-based digital-light-processing (DLP) projector, which suffers from the limitations such as the requirement of precise synchronization, speed limit of measurement, and the nonlinear gamma effect of the DLP projection [14]. For the laser-based DLP projector, it still uses a DLP chipset, but its light source is laser-based instead of light-based. Thus, the laser-based DLP projector also has the drawbacks of a traditional DLP projector as we discussed above. Moreover, the most existing techniques based on those encoding methods may have the rigorous requirement that the vibration caused by the surrounding environment and the background illumination are mostly not allowed during the measurement, which indicates that outdoor in-situ measurements and reconstruction of usual objects being observed will be impossible. We have noticed that the recently developed stereo-vision-based

Manuscript received November 10, 2021; revised December 29, 2021; accepted January 11, 2022. Date of publication January 14, 2022; date of current version January 26, 2022. This work was supported in part by the Shandong Province Higher Educational Science and Technology Program under Grant J18KZ012, in part by the National Natural Science Foundation of China under Grant 11975132, in part by the Natural Science Foundation of Shandong Province under Grants ZR2016FB09 and ZR2019BF050, and in part by the Natural Science Foundation of Shandong Province for Excellent Young Scholars under Grant ZR2019YQ01. *(Bingquan Chen and Peng Shi contributed equally to this work.) (Corresponding author: Hongsheng Li.)*

Bingquan Chen, Peng Shi, Hongsheng Li, Hongxiu Gao, Peng Gao, Xufei Wu, and Jun Yue are with the School of Science, Qingdao University of Technology, Qingdao 266525, China (e-mail: chen_bingquan@yeah.net; shipeng@qut.edu.cn; lihongsheng1123@qut.edu.cn; gaohongxiu@qut.edu.cn; gaopeng20210327@163.com; wuxufei0033@163.com; yuejun@qut.edu.cn).

Ruirong Wang is with the Office of Laboratory Management, Qingdao Agricultural University, Qingdao 266109, China (e-mail: 199201019@qau.edu.cn).

Digital Object Identifier 10.1109/JPHOT.2022.3143116

method for the measurement and reconstruction of a dynamic object illuminated by structured light [15]–[17]. This method based on the single-shot measurement and the projection of red-green-blue (RGB) line pattern or RGB dot pattern indicated the feasibility of measuring a dynamic target under complicated environmental conditions.

The outdoor applications of law-enforcement related work may include the measurement and reconstruction of crime scene [18], [19], cultural heritage investigation [20], [21], measuring the shape and position of a moving object or creature [22], global measurement of free surface deformations [23], and target recognition [24], [25]. The varying environmental conditions related to outdoor applications including the background illumination, wind, rain, and fog will be critically challenging for carrying out accurate measurements and reconstructions of the observed objects using structured-light-based methods. It was recently reported that a TOF method was developed by Kijima and co-workers for measuring the depth and intensity [26]. Even this approach was expected to work for any thin scattering media, its resolution is still limited by the general TOF technique. Another structured-light-based technique was recently reported by Shi and co-authors, and this 20-μm-resolution 3D microscopic imaging method showed the possibility of outdoor application for measuring and monitoring surface deformations such as bridge and road crack [27].

However, to the best of our knowledge, there has not been any developed method that is based on the structured-light projection for 3D imaging and reconstruction under rainy conditions. A successful method of in-situ measurement and reconstruction using structured light under rainy conditions should be capable of solving the following problems: (i) The coded structured pattern used for in-situ measurement and reconstruction under rainy conditions has to keep the designed and accurate coded structured form, e.g. the purely sinusoidal fringe pattern, after its propagation in the rain, which should not be affected by spectral absorption, multiple scattering, and other physical processes. (ii) The effects of background illumination and multiply-scattered light have to be removed accurately. (iii) The effect of vibration from environmental influences including the structural vibration of the system and the air disturbance has to be eliminated. (iv) The background medium containing rain is not homogeneous due to the time-variant environmental conditions, which might be difficult for developing physical model of imaging and reconstruction, such as the model based on TOF method by Kijima *et al.* [26]. The fundamental feature of the DLP-based structured light is that the output fringe pattern is an image that needs to be focused on the focal plane where the observed target is located, which is different from the basis of our proposed method. Since the optical signal of the output fringe pattern generated by DLP is incoherent, it is difficult to remove the incoherent noised signal from background illumination and multiple scattering for carrying out outdoor measurement. Thus, the technique using the projection of DLP-based structured light might be difficult to fulfill the task of in-situ 3D measurement and reconstruction under rainy conditions, since coded structured pattern will be modulated and affected by the non-uniform spectral attenuation through the water [28], multiple scattering, focusing of the object being observed, precise synchronization, and the speed limit of measurement.

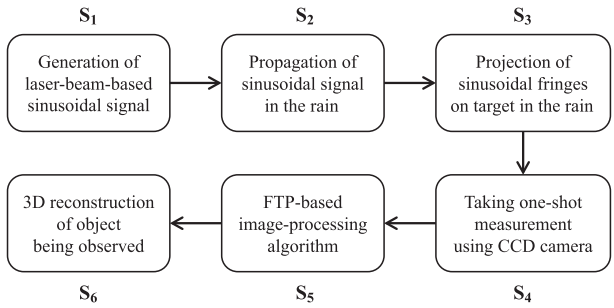

Fig. 1. Flowchart of the proposed method for 3D imaging and reconstruction of objects being observed in the rain.

Thus, the goal of this work is to propose and develop a method with a designed laser-beam-based optical system for generating the monochromatic structured light, techniques of optical filtering and polarization, and the image-processing algorithm based on one-shot Fourier transform profilometry. The developed method will be analyzed theoretically and investigated experimentally for the 3D measurement and reconstruction under rainy conditions.

II. Description and Analysis of the Proposed Method for 3D Imaging in the Rain

A flowchart of the proposed method for 3D imaging and reconstruction of objects being observed under rainy conditions is demonstrated in Fig. 1. The major aspects in accordance with the proposed method are analyzed and discussed as follows.

A. The Designed Optical Set-Up for Generating Sinusoidal Signal

The sinusoidal-signal generation, noted as S_1 in Fig. 1, is realized using the optical set-up in the lower part of Fig. 2(a). The designed optical set-up mainly contains the following four components: (i) A continuous-wave (CW) laser source with the wavelength $\lambda = 532$ nm, maximum output power of 200 mW, and a divergence angle $\leq 1.5^{\circ}$. (ii) A positive lens, used for the function of Fourier transform. (iii) A rectangular grating, illuminated by the laser beam and located at a front focal point of a positive lens. (iv) An adjustable spatial-frequency filter placed on the conjugate plane of laser source. Note that, this spatial-frequency filter has a V-shape aperture with precise width of 0.5 mm, which is critically important for the selected order of the spatial frequency to pass through. The detailed mathematical description and equation derivation of the process from the laser source to the observed object will be given in Section III below.

B. Artificially-Created Raining Environment

The raining environment was artificially created as shown in Fig. 2(a). In Fig. 2, the size of the region covered by the rain was $13.5 \times 7.5\ (m)$. The rainfall of the artificially-created rain was adjusted between $0 \sim 150\ (mm/hour)$, while a scaled cylindrical cup was used as rain gauge for measuring the rainfall.

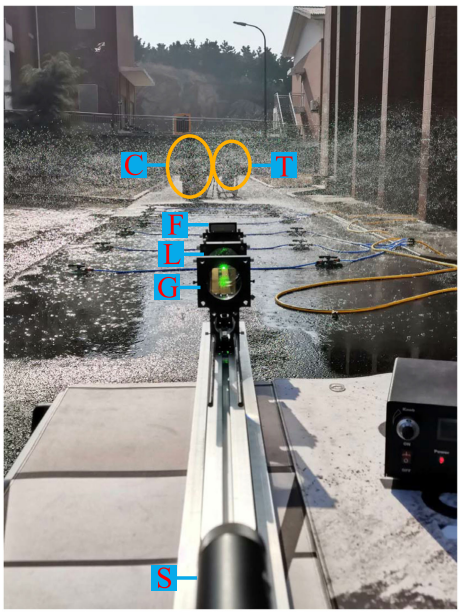

(a)

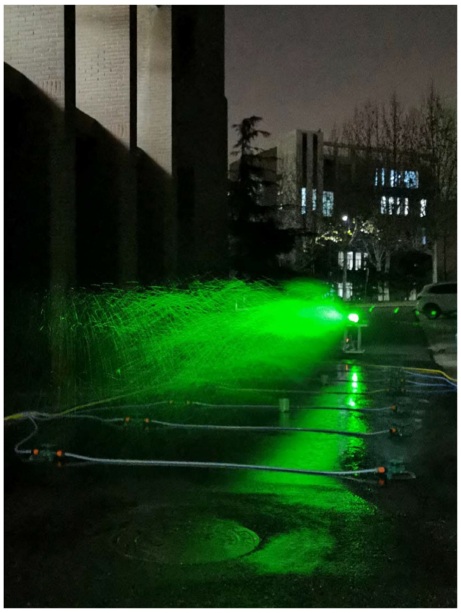

(b)

Fig. 2. Photo of the experimental setup including the developed the laser-beam-based optical system and the target being measured in the artificially-created rain. S: CW laser source; G: grating; L: Fourier-transform positive lens; F: spatial-frequency filter; P: observation plane; T: target on the observation plane; C: CCD Camera connected to a computer. (a) The photo was taken when the measurement were carried out in the daytime. (b) The photo was taken when the measurement were carried out in the evening.

It should be noted that there also were two real-time parameters to be measured during the period of in-situ experimental measurement, the wind speed v (m/s) measured using a digital anemometer and the background illuminance E (Lux) measured using a digital luxmeter. The laser-beam-based sinusoidal optical signal and its propagation in the rain as well as the related method of 3D measurement and reconstruction under rainy condition will be analyzed and discussed in the following parts.

C. Propagation of Laser-Beam-Based Sinusoidal Signal in a Random Medium

The effect of spectral absorption makes it clear that the projection of DLP-based structured light is unable to fulfill the task of 3D imaging and reconstruction of objects located in absorbing and scattering media, such as rain, fog, and turbid water. The main reason for selecting the CW laser source at 532 nm is that the water absorption coefficient at 532 nm is much lower comparing to the yellow-red region (580–700 nm) [29], [30]. Previous studies of imaging through scattering media [26], [31], [32] have demonstrated that the multiple-scattering process should dominate the optical signal propagation in the scattering medium like the rain. For the purpose of optical communication, the pulsed-laser propagation in the rain has been investigated theoretically and experimentally [33]–[36], which may provide a part of the physical basis for considering and designing the experimental frame of this work. The key theoretical consideration of our approach is based on the multiple scattering theory [37], which is briefly discussed as follows.

Starting from a CW point laser source, the propagating field in a random medium, $U(r)$, has the form [38]

$$U(r) = \frac{A}{r}\mathrm{e}^{iKr}, \tag{1}$$

where A is a complex constant related to the laser power, and $r = \sqrt{x^2 + y^2 + z^2}$. K is the wave number in the homogeneous background medium, and it can be written as

$$K = k + ik_0, \tag{2}$$

where k is the real part of K, being the wave number of the field from the laser source in vacuum or air, and k_0 is the imaginary part of K, representing the attenuation by the random medium.

The field $U(r)$ within the range of the random medium, i.e. the region covered by the rain, is a random function of r and can be divided in a coherent field $U_c(r)$, also called the effective field, and an incoherent field $U_{inc}(r)$, also called the fluctuating field. $\mid U_c(r) \mid^2$ is called the coherent intensity $I_c(r)$, and the average of the square of the incoherent field amplitude $<\mid U_{inc}(r) \mid^2>$ is called the incoherent intensity $I_{inc}(r)$. The total intensity $I(r)$ is the sum of the coherent and the incoherent intensity, i.e.

$$I(r) = \mid U(r) \mid^2 = \mid U_c(r) \mid^2 + <\mid U_{inc}(r) \mid^2> . \tag{3}$$

Considering the condition that the divergence angle of the CW laser source is $\leq 1.5^\circ$ as well as the paraxial approximation, on propagation in the random medium the propagating coherent field is attenuated due to scattering and absorption [37], [39], i.e.

$$U_c(r) = \frac{Ae^{-k_0 z}}{r}\mathrm{e}^{ikr}. \tag{4}$$

Note that, $U_c(r)$ is the basis for the generation of laser-beam-based sinusoidal signal under rainy conditions of our approach, while the incoherent intensity consisting the multiply-scattered photons and background illuminance will be eliminated by using polarizer and optical filter.

The coherent intensity I_c, the square of the coherent field amplitude, is attenuated due to scattering and absorption [37]

$$I_c = I_{c0}\mathrm{e}^{-\mu z}, \tag{5}$$

where I_{c0} is the intensity of propagating field in the air, the extinction coefficient $\mu = \sigma_s + \sigma_a$, and σ_s and σ_a are the scattering and absorption coefficients, respectively. Thus, the imaginary part of K is given by combining (4) and (5)

$$k_0 = \frac{\mu}{2}, \tag{6}$$

while μ is measurable in practical experiments.

Note that, the extinction coefficient μ in (5) is dominated by the scattering process of rain drops at 532 nm [40], [41], which means that $\sigma_a \approx 0$ and $\mu \approx \sigma_s$ at the wavelength that we have used in this work. The calculation of σ_s is based on the data of rain-drop-size distribution and the cross section, while such statistical data is difficult to obtain due to the varying rainfall and dynamic environmental conditions.

D. Eliminating Incoherent Noised Signal $I_{inc}(r)$ and Background Illuminance $I_b(r)$

The field $U_{inc}(r)$ is incoherent and depolarized, which results from the multiple scattering of photons of the propagating laser-beam-based sinusoidal signal generated by the designed optical system at 532 nm. The component $I_{inc}(r) =< \mid U_{inc}(r) \mid^2 >$ can be clearly identified in Fig. 2(b), and the color green of the whole rainy region stands for the distribution of $I_{inc}(r)$ as shown in Fig. 2(b), while the background illuminance $E \approx 0$ due to the dark environment as the photo was taken in the evening. Obviously, the value of fluctuating $I_{inc}(r)$ depends on the propagating laser-beam-based sinusoidal signal, the rainfall, and other physical parameters of the measuring system and environment.

As we discussed above, the desired useful signal is $I_c(r)$ in the approach of this investigation, while $I_{inc}(r)$ is then taken as noised signal to be eliminated. Rigorously speaking, in addition to $I_c(r)$ and $I_{inc}(r)$, there should also be $I_b(r)$, i.e. the intensity of background illumination. Note that both $I_c(r)$ and $I_{inc}(r)$ only have the non-zero values at 532 nm, but $I_b(r)$ is measurable at all of the wavelengths of visible-light spectrum. The effect of background illumination, i.e. $I_b(r)$, can be eliminated using an optical bandpass filter centered at 532 nm with full width at half maximum (FWHM) being 20 nm. The component $I_{inc}(r)$ is capable of being eliminated via employing polarization technique, which can be ensured since the incident monochromatic structured light and reflected signal from the surface of the translucent objects being observed are linearly polarized, and the part of signal composing multiply-scattered photons is completely unpolarized. When carrying out the practical measurement, both the optical bandpass filter and the polarizer mentioned above are mounted on the measuring camera.

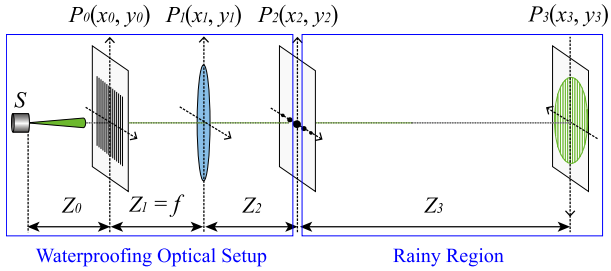

Fig. 3. The generation and propagation of the sinusoidal optical signal. S: CW laser source; P_0: the plane of grating; P_1: the plane of Fourier-transform lens; P_2: the plane of spatial-frequency filter, and it coincides with the interface between the air region and the rainy region; P_3: the observation plane.

E. Fourier-Transform-Based Measurement and Reconstruction

Reconstruction of the object being observed will be processed and obtained using the one-shot measurement based on Fourier transform profilometry (FTP). The method of FTP was initiated by Takeda and Mutoh [7], and it has been applied and improved in many investigations of 3D surface measurement [42]–[45]. The reflectance of $I(x_3, y_3) = I(x_3)$, as described in (16) and (17) below, is to be measured, and x_3 is the only variable in the expression of $I(x_3, y_3)$ at the object plane along x_3-axis for describing the illuminated fringe patterns. Image-processing algorithm for the retrievals of phase and 3D-surface height using the measured reflectance of $I(x_3, y_3)$ is based on FTP with a typical triangulation framework of 3D surface measurement, while the general framework and theoretical basis of Fourier-transform-based 3D surface measurement and reconstruction can be found in previous works published by Takeda and Mutoh [7] and by Maurel and co-workers [42].

III. Generation of the Laser-Beam-Based Sinusoidal Fringe Signal and Its Propagation in the Rain

This section presents the theoretical analysis and mathematical description of the generation and propagation of the sinusoidal fringe signal generated using the designed laser-beam-based optical system and the propagation of the sinusoidal fringe signal in the rain. For in-situ measurement under rainy conditions, the sinusoidal optical signal generator that mainly contains parts S, G, L, F, and the optical rail as shown in Fig. 2(a) can be placed in waterproof housing, which is sketched in Fig. 3. From Fig. 3 we see that the plane P_2 is right before the interface between the air region and the rainy region, and the observation plane P_3 is located in the rain. In the designed optical setup sketched in Fig. 3, $Z_0 + Z_1 + Z_2 = 0.75$ m, while Z_3 can be any value between 1$\sim$30 m.

A. The Field From the CW Point Laser Source S to the Spatial-Frequency Filter At Plane P_2

The grating G is illuminated by the coherent field from the CW point source laser S. Based on the paraxial approximation and propagation theory within the Fresnel region, the field $U_1(x_1, y_1)$ right behind the lens L at the plane P_1 can be written

as [24]

$$U_1(x_1,y_1) = C_1 \mathrm{e}^{-i\frac{k}{2f}(x_1^2+y_1^2)} \int_{\Sigma_0} U_0(x_0,y_0) \times \mathrm{e}^{i\frac{k}{2Z_1}[(x_1-x_0)^2+(y_1-y_0)^2)]} dx_0 dy_0, \quad (7)$$

where $C_1 = \frac{1}{i\lambda Z_1}\mathrm{e}^{ikZ_1}$ is a complex constant, Z_1 is the distance between the planes P_0 and P_1, $t_L(x_1,y_1) = \mathrm{e}^{-i\frac{k}{2f}(x_1^2+y_1^2)}$ is defined as the transmission function of the lens L, $U_0(x_0,y_0)$ is the field behind the grating G at the plane P_0, i.e.

$$U_0(x_0,y_0) = \frac{1}{Z_0}\mathrm{e}^{ikZ_0}\mathrm{e}^{i\frac{k}{2Z_0}(x_0^2+y_0^2)} t_0(x_0,y_0),$$

with the transmission function of G being

$$t_0(x_0,y_0) = t_0(x_0) = \left[\mathrm{rect}\left(\frac{x_0}{a}\right) * \frac{1}{d}\,\mathrm{comb}\left(\frac{x_0}{d}\right)\right] \mathrm{circ}\left(\frac{2|x_0|}{H}\right),$$

where a and d are the optical parameters of grating G, and H is the grating width. Note that H is assumed to be the diameter of the illumination spot of laser in this study.

Fresnel diffraction can be applied to the propagation of $U_1(x_1,y_1)$ from plane P_1 to plane P_2. The field $U_2'(x_2,y_2)$ in front of the spatial-frequency filter F at plane P_2 is then given by

$$U_2'(x_2,y_2) = C_2 \int_{\Sigma_1} U_1(x_1,y_1) \times \mathrm{e}^{i\frac{k}{2Z_2}[(x_2-x_1)^2+(y_2-y_1)^2)]} dx_1 dy_1, \quad (8)$$

where $C_2 = \frac{1}{i\lambda Z_2}\mathrm{e}^{ikZ_2}$ is a complex constant, and Z_2 is the distance between the planes P_1 and P_2. Based on (7) and (8) as well as the expressions of $t_0(x_0,y_0)$ and $t_L(x_1,y_1)$, $U_2'(x_2,y_2)$ will have the form

$$U_2'(\omega) = \frac{aC_2'}{d}\sum_{m=-\infty}^{\infty} \mathrm{sinc}\left(\frac{am}{d}\right) \frac{\mathrm{J}_1[\pi H(\omega - m/d)]}{\omega - m/d}, \quad (9)$$

where $\mathrm{J}_1(\omega)$ is the Bessel function of the first kind, $\omega = 2\pi f_x$ with the spatial frequency f_x at plane P_2 defined by $f_x = \frac{x_2}{\lambda f}$, and C_2' is a complex constant given by $C_2' = \frac{1}{\lambda f Z_0}\mathrm{e}^{i[k(Z_0+Z_1+Z_2)-\pi/2]}$.

Actually, the spatial-frequency filter on the plane P_2 in Fig. 3 is a V-shape aperture with a width of 0.5 mm that has been carved with high precision. In this designed spatial-frequency filter, a V-shape aperture overlaps with a bar-shape aperture. The horizontal bar-shape aperture crosses the V-shape aperture, which results in two little apertures with the hole size of 0.5 mm. The horizontal bar-shape aperture can be adjusted via moving up and down for matching the positions of $\pm m$-th order spectra described in (9). Thus, the role of the adjustable spatial-frequency filter F at plane P_2 is to select a pair of $\pm m$-th order spectra, and let them to pass through it. In this investigation, we take $m = 1$. Thus, the field $U_2(x_2,y_2)$ right behind the filter F can be written as

$$U_2(x_2,y_2) = U_2'(\omega)\big|_{m=\pm 1} = \frac{aC_2'}{d}\mathrm{sinc}\left(\frac{a}{d}\right)\left\{\frac{\mathrm{J}_1[\pi H(\omega-1/d)]}{\omega-1/d} + \frac{\mathrm{J}_1[\pi H(\omega+1/d)]}{\omega+1/d}\right\}. \quad (10)$$

B. The Field Propagation in the Rain: From the Air-Rain-Interface Plane P_2 to the Observation Plane P_3

The propagation of field $U_2(x_2,y_2)$ from plane P_2 to P_3 can also be described using Fresnel diffraction, and the field $U_3(x_3,y_3)$ at plane P_3 is given by

$$U_3(x_3,y_3) = C_3 \int_{\Sigma_2} U_2(x_2,y_2) \times \mathrm{e}^{i\frac{K}{2Z_3}[(x_3-x_2)^2+(y_3-y_2)^2)]} dx_2 dy_2, \quad (11)$$

where $C_3 = \frac{1}{i\lambda Z_3}\mathrm{e}^{iKZ_3}$ is a complex constant, and Z_3 is the distance between the planes P_2 and P_3. Note that the complex wave number K used in (11) as well as the expression of C_3 is defined in (2).

The complex constant C_3 can be written as $C_3 = \frac{1}{i\lambda Z_3}\mathrm{e}^{ikZ_3}\mathrm{e}^{-\frac{\mu}{2}Z_3}$ based on (2) and (6), while the term $\mathrm{e}^{-\frac{\mu}{2}Z_3}$ represents the attenuated amplitude of the propagation field comparing to the case of propagation in the air. We can also rewrite (11) as

$$U_3(x_3,y_3) = C_3 \int_{\Sigma_2} U_2(x_2,y_2)\mathrm{e}^{-\frac{\mu}{4Z_3}[(x_3-x_2)^2+(y_3-y_2)^2)]} \times \mathrm{e}^{i\frac{k}{2Z_3}[(x_3-x_2)^2+(y_3-y_2)^2)]} dx_2 dy_2, \quad (12)$$

where we may need to present the analysis for taking two assumptions:

(i) The first assumption $\mathrm{e}^{-\frac{\mu}{4Z_3}[(x_3-x_2)^2+(y_3-y_2)^2]} \approx \mathrm{e}^0 = 1$: Considering that the typical value of the extinction coefficient $\mu = 0.001 \sim 0.02\ (m^{-1})$ in accordance with different values of rainfall, $x_3 = y_3 \approx 0.1 \sim 0.5\ (m)$, $Z_3 \approx 10 \sim 50\ (m)$, thus $\frac{\mu}{4Z_3}[(x_3-x_2)^2+(y_3-y_2)^2] \approx 10^{-4} \sim 10^{-7} \approx 0$.

(ii) The second assumption $\lambda f(f_x^2+f_y^2) \ll 2(f_x x_3 + f_y y_3)$: Considering that the size of $\Sigma_2(x_2,y_2)$ ($\leq 4\ mm$ in diameter) is much less than that of $\Sigma_3(x_3,y_3)$, i.e. the spot size of the sinusoidal fringe pattern on the observation plane P_3 ($\geq 100\ mm$ in diameter), the approximation that $\lambda f(f_x^2+f_y^2) \ll 2(f_x x_3 + f_y y_3)$ should be valid.

Thus, the optical field at the observation plane P_3 can be derived using (12) together with those two assumptions above, i.e.

$$U_3(x_3,y_3) = C_3' \int_{\Sigma_2} U_2(f_x,f_y)\mathrm{e}^{i2\pi(f_x\frac{f x_3}{Z_3}+f_y\frac{f y_3}{Z_3})} df_x df_y = C_3'\mathcal{F}^{-1}\{U_2(f_x,f_y)\}, \quad (13)$$

where $C_3' = \frac{\lambda f^2}{Z_3}\mathrm{e}^{-\frac{\mu}{2}Z_3}\mathrm{e}^{i[kZ_3-\pi/2]}\mathrm{e}^{i\frac{k}{2Z_3}(x_3^2+y_3^2)}$ and $f = Z_1$ is the focal length of the lens. It should be noted that the rain-model effect is reflected by the parameter μ in the expression of C_3'.

Equation (13) indicates that the field at the observation plane P_3 is an inverse Fourier transform of the field output from the

spatial-frequency filter F. Combining (10) and (13), we have

$$U_3(x_3) = C \cdot \mathrm{circ}\left(\frac{2f|x_3|}{HZ_3}\right) \cdot \cos\left(\frac{2\pi f x_3}{dZ_3}\right), \quad (14)$$

where

$$C = \frac{2f}{Z_0 Z_3 \pi} \sin\left(\frac{a\pi}{d}\right) \mathrm{e}^{-\frac{\mu}{2}Z_3} \mathrm{e}^{i[k(Z_0+Z_1+Z_2+Z_3)-\pi]} \times \mathrm{e}^{i\frac{k}{2Z_3}(x_3^2+y_3^2)}. \quad (15)$$

Obviously, C is a complex constant for determined spatial distances Z_0 and Z_3, and the modulus of C represents the amplitude of the generated sinusoidal signal. We see that the fringe intensity will decrease as Z_3 increases since f and Z_0 are generally parameters with fixed values. The part of $\mathrm{circ}(\frac{2f|x_3|}{HZ_3})$ in (14) results in a definition of the range of the fringe pattern with a circle of radius $\frac{HZ_3}{2f}$. The term of $\cos(\frac{2\pi f x_3}{dZ_3})$ is the key part of output of the designed optical system, i.e. the expression of a sinusoidal curve.

We see from (14) that the field $U_3(x_3, y_3)$ at the observation plane P_3 is an inverse Fourier transform of the field output from P_2, i.e. the plane of spatial-frequency filter. (14) can be rewritten as

$$U_3(x_3) = C_r \cdot C_i \cdot \mathrm{circ}\left(\frac{2f|x_3|}{HZ_3}\right) \cdot \cos\left(\frac{2\pi f x_3}{dZ_3}\right), \quad (16)$$

where the real part C_r and imaginary part C_i of the complex constant C are given by, respectively,

$$C_r = \frac{2f}{Z_0 Z_3 \pi} \sin\left(\frac{a\pi}{d}\right) e^{-\frac{\mu}{2}Z_3},$$

$$C_i = \mathrm{e}^{i[k(Z_0+Z_1+Z_2+Z_3)-\pi]} \mathrm{e}^{i\frac{k}{2Z_3}(x_3^2+y_3^2)}.$$

We see from (16) that C_r is a real constant for fixed spatial distances, and it represents the term of amplitude. The amplitude will decrease for two reasons: one is the increase of Z_3, the other is the extinction due to the absorption and scattering of the rain, i.e. the effect of parameter μ. The $circ-$function in (16) defines the range of the fringe pattern with a circle of radius $\frac{HZ_3}{2f}$. The $cosine$ term in (16) has only one variable x_3 at the plane P_3 along x_3-axis, which indicates that the output of this system is monochromatic, high contrast, and truly sinusoidal fringes. The $cosine$ term also includes the information that the fringe width (related to the spatial frequency of the output fringe pattern) will increase as Z_3 increases, which might be useful and important for 3D surface measurement.

The intensity distribution of the projected fringe pattern on the observation plane, i.e. P_3 in Fig. 3, is given by

$$I(x_3, y_3) = U_3(x_3, y_3) U_3^*(x_3, y_3) = U_3(x_3) U_3^*(x_3), \quad (17)$$

where $U_3(x_3)$ is given in (16), and $U_3^*(x_3)$ is the conjugate of $U_3(x_3)$. Note that $U_3(x_3)$ has been being coherent until reaching the surface of the observed target on the observation plane, and $I(x_3, y_3)$ represents the high-contrast sinusoidal fringe pattern when the incoherent noised signal I_{inc} and background illuminance I_b are removed. Even $I(x_3, y_3)$ is a function of Z_3, it keeps being high-contrast for all values of Z_3 without any defocusing issue. $I(x_3, y_3)$ is modulated by the surface height of the target, which will result in the deformed $I(x_3, y_3)$, i.e. the deformed sinusoidal fringe pattern, on the surface of the 3D object being observed. The reflectance of the deformed $I(x_3, y_3)$, i.e. the image of the deformed sinusoidal fringe pattern on the target, will be measured by the camera, which will be used for phase retrieval of surface height and 3D reconstruction of the object being observed.

IV. Experimental Results of In-Situ Measurements in the Rain

The experimental results presented in this section was completed using the outdoor frame of 3D surface measurement as shown in Fig. 2. The measurement was lasting from 3 to 9 PM for obtaining different measuring results in accordance with different parameters of environmental condition, such as different values of background illuminance. During the measuring period, the rainfall of the artificially-created rain was controlled to be 120 $mm/hour$. The wind speed v was measured using a digital anemometer and recorded as $v = 1.0 \sim 5.5\ m/s$, and the varying background illuminance E was measured right before each measurement of the observed object as indicated in the captions of Figs. 4 and 6. We should point out that both the wind speed v and the background illuminance E are used to represent the environmental condition in our investigation. Both v and E are not the necessary parameters needed to be used for image processing and reconstruction, even they are critically important for most other structured-light-based techniques. The extinction coefficient μ was measured using HR2000+ spectrometer, and $\mu = 0.008\ (m^{-1})$ for the rainfall of 120 $mm/hour$ for the situation of the artificially-created rain in this work. Note that, for all of the measurements, an optical polarizer and an optical bandpass filter centered at 532 nm with FWHM being 20 nm were employed.

A. Measurement and Reconstruction of the Dynamic Human Face in the Rain

In this part of experiment, a dynamic human face was illuminated by a monochromatic sinusoidal fringe pattern generated using our designed optical system at 532 nm, while the spatial frequency of the sinusoidal fringe pattern is 1.0 lp/mm. The selected images and related reconstructions are shown in Fig. 4.

The images in Fig. 4(a), (c), and (e) represent the measurements of the human face illuminated by monochromatic sinusoidal fringe pattern at 532 nm at different background illuminance E, and the image of Fig. 4(a) was taken in the air with $E = 0$, the image of Fig. 4(c) was captured in the rain with $E = 0$, and the image of Fig. 4(e) was obtained in the rain with $E = 500\ Lux$, respectively. It should be pointed out that the human face did not need to keep being stable, and face shaking and moving was allowed during the measuring time. In addition to seeing the fringes on the face, we can also identify water drops on the face from Fig. 4(c) and (e).

The images in Fig. 4(b), (d), and (f) represent the reconstructions of 3D surface shape image or topography of the human face using the measurements of Fig. 4(a), (c), and (e), respectively.

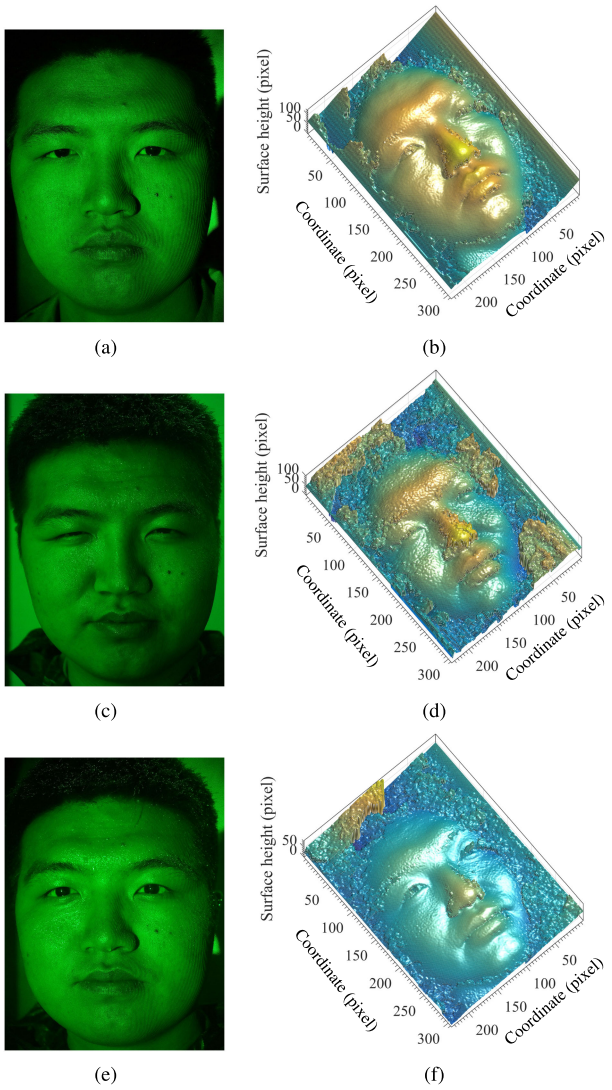

Fig. 4. Measurement and reconstruction of the human face in the rain, and the background illuminance is E. (a) Image in the air with $E = 0$. (b) Reconstruction using (a). (c) Image in the rain with $E = 0$. (d) Reconstruction using (c). (e) Image in the rain with $E = 500\ Lux$. (f) Reconstruction using (e).

From Fig. 4(d) and (f) we see that accurate reconstructions of dynamic human face based on the measurements in the rain with rainfall of 120 $mm/hour$ could be obtained. Especially, we could obtain accurate reconstruction for measuring the 3D surface shape of a moving human face even when background illuminance exists, as indicated in Fig. 4(f). We also have noted that the little decrease of the accuracy of reconstruction via comparing Fig. 4(d) and (f) with Fig. 4(b), and the reason of such a decrease might mainly include (i) the decrease of the fringe contrast due to the extinction and multiple scattering by rain drops, and (ii) the reflection and refraction of projected light by water drops on the face in the rain. As far as the noised background region around the human face in Fig. 4(b) is concerned, we should point out that Fig. 4(b) is obtained based on Fig. 4(a), and there is a one-pixel to one-pixel correspondence. Thus, if we want to have a clear background, the only way is to cut off the surrounding background before processing the image.

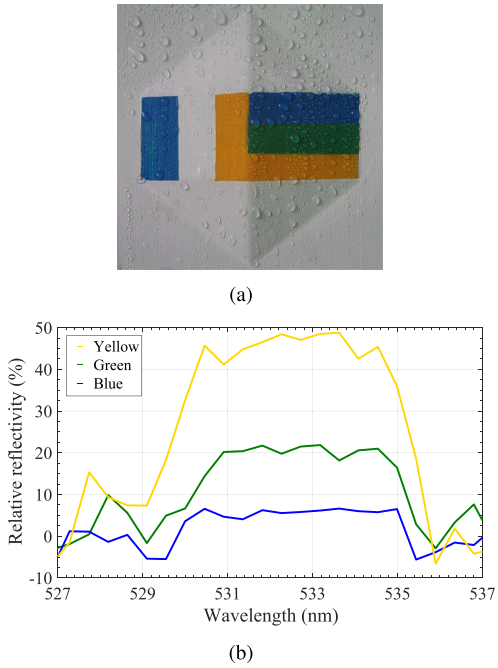

Fig. 5. The designed 3D-printed color object and its surface reflectivity. (a) Photo of the heptahedron-shape object, taken on the experimental site in the rain. (b) The measured color-dependent surface reflectivity of the color object at 532 nm.

B. Measurement and Reconstruction of a Designed Color Object in the Rain

Aiming at investigating the accuracy of reconstruction for measuring 3D objects in the rain, a designed 3D-printed color object was used as observed target. This color object had the heptahedron shape and was designed with given geometrical parameters, which would be used for determining the accuracy of reconstruction. The heptahedron-shape object had the shape similar to an elongated triangular dipyramid, while it was initially generated using a 3D printer and then coated with the same type of paint but with different colors, as shown in Fig. 5(a). As described in Fig. 5(b), the color object has color-dependent surface reflectivity at 532 nm. Figure 5(b) indicated that, if the perpendicular reflectivity of the white-color region of the object surface in Fig. 5(a) was taken as unity, the reflectivities of the yellow, green, and blue regions of Fig. 5(a) would be about 48%, 20%, and 5%, respectively.

The color object was also illuminated by a monochromatic sinusoidal fringe pattern generated using our designed optical system at 532 nm, and the spatial frequency of the sinusoidal fringe pattern was adjusted to 2.0 lp/mm. The reconstructive 3D images of the color object in Fig. 6(b), (d), and (f) were obtained using the measurements of Fig. 6(a), (c), and (e), respectively, which showed that the reconstruction based on the measurement of the color object in the rain as indicated in Fig. 6(d) and (f) would be capable of yielding the same accuracy as the result of Fig. 6(b), i.e. the reconstruction using the measurement without rain. The plots in Fig. 7 can be employed for analyzing the accuracy of reconstruction of the proposed method.

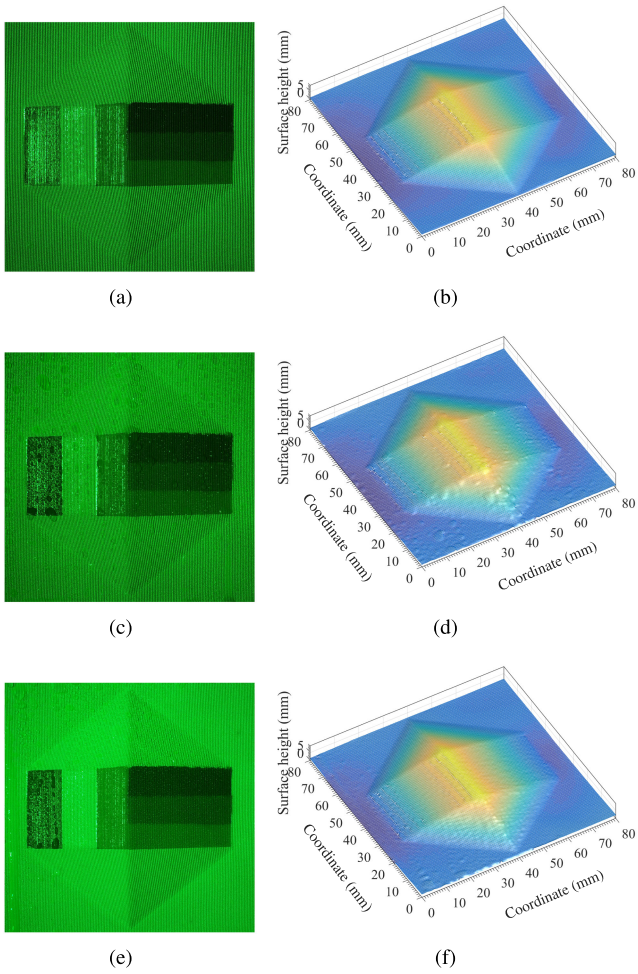

Fig. 6. Measurement and reconstruction of the designed color object in the rain, and the background illuminance is E. (a) Image in the air with $E = 0$. (b) Reconstruction using (a). (c) Image in the rain with $E = 0$. (d) Reconstruction using (c). (e) Image in the rain with $E = 500\ Lux$. (f) Reconstruction using (e).

The error of reconstruction was described in the plots of Fig. 7, and the accuracy of reconstruction was based on the comparison between the retrieved height distribution on the cross sections perpendicular/parallel to the ridge and the actual geometrical parameters of the designed color object generated using 3D printer. The result of Fig. 7 may indicate that an accurate reconstruction can be obtained using 3D surface-shape measurement of the object with varying surface reflectivity under rainy condition via the combination of laser-beam-based structured light, the optical filtering, and the polarization technique.

To quantitatively evaluate difference between known and calculated geometry of the object being observed, we employ the root mean square error (RMSE) for telling the accuracy of reconstruction. Generally speaking, the lower the RMSE, the better the accuracy of the reconstruction. With sampling points $N = 86$, the calculated RMSE using the data of Fig. 7(b) and Fig. 7(d) are, respectively,

$$\sigma_{\text{perp}} = \sqrt{\frac{1}{N}\sum_{i=1}^{N}(x_i - \bar{x})^2} = 0.161\ (mm),$$

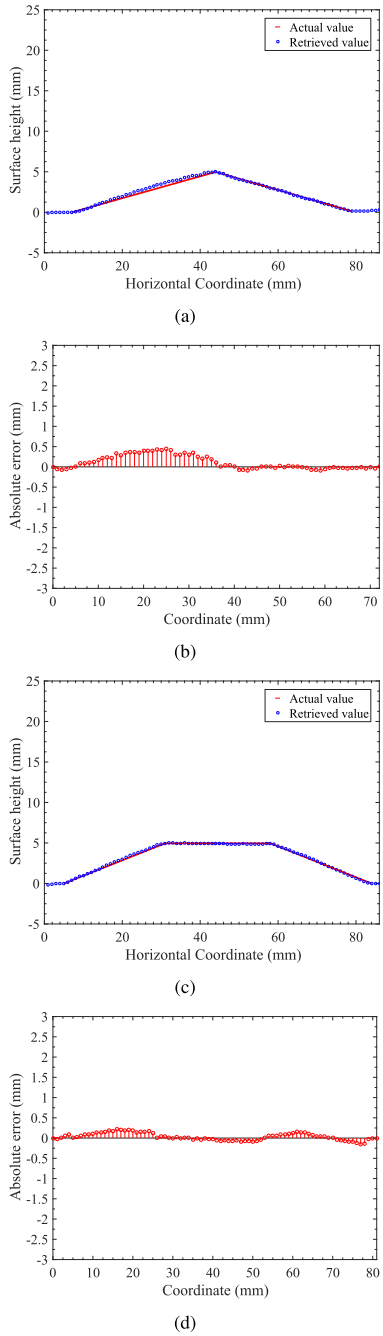

Fig. 7. Comparing the retrieved height distribution with actual values based on the data of Fig. 6. (a) Comparing the retrieved height distribution on the cross section perpendicular to the ridge with actual values. (b) The absolute-error distribution of retrieved surface height in accordance with (a). (c) Comparing the retrieved height distribution on the cross section parallel to the ridge with actual values. (d) The absolute-error distribution of retrieved surface height in accordance with (c).

$$\sigma_{\text{para}} = \sqrt{\frac{1}{N}\sum_{i=1}^{N}(x_i - \bar{x})^2} = 0.093\ (mm).$$

Note that the region on the surface of the heptahedron-shape object with relative big reconstruction error is partially due to the actual shape defect formed when the object was created using

the 3D printer. We can see the pimples on the surface of the reconstructed objects in Fig. 6(d) and (f), which is considered as being due to the water drops on the surface of the observed object in the rain as indicated in Fig. 5(a). As we mentioned above, reflection and refraction by the water drops will result in the distortion of the reflected fringes, which should be the main reason of resulting in the pimples on the surface of the reconstructed object in accordance with the locations of the water drops on the object being observed.

We can also see that it is hard to tell the difference between Fig. 6(b) and (f), i.e. the reconstructions from the measurement in the air and that in the rain, respectively. Based on the data of Fig. 6(b), the calculated RMSEs of the same cross sections as Fig. 7 are $\sigma_{\mathrm{perp}}^{\mathrm{air}} = 0.110\ (mm)$, $\sigma_{\mathrm{para}}^{\mathrm{air}} = 0.075\ (mm)$, which looks slightly better. Obviously, the reason of the accuracy decrease of the reconstruction of Fig. 6(f) comparing to the result of Fig. 6(b) is the rain.

C. Discussions

It is noticed that the optical filtering technique should play an important role if the background illumination exists for the measurements in Figs. 4(e) and 6(e), which is determined by the monochromaticity of the projected sinusoidal fringe pattern.

The ability of the proposed method for measuring a dynamic human face in the rain, measuring a color object with varying reflectivity in the rain, and obtaining accurate reconstructions of the observed objects in the rain has been described and confirmed with those experimental results completed in this study. The accuracy of reconstruction is ensured by all aspects discussed above, mainly including the physical feature and accuracy of the projected fringe pattern generated using the designed laser-beam-based optical system, the optical filtering and polarization techniques and the one-shot FTP-based imaging processing algorithm. Note that the projected structured light with the optical wave from laser source is monochromatic and generally polarized, thus both the optical filtering and polarization techniques can be used for measurement and image processing as we have proposed in our investigation. However, since the optical signal generated by a DLP-based projector is non-monochromatic and unpolarized, it is impossible to extend our approach to the methods and applications that are based on the use of structured light generated by a DLP projector.

It should be noted that the accuracy of 3D measurement and reconstruction of the observed objects in the rain is basically determined by the intensity, contrast, and spatial frequency of the projected fringes and the background illumination. The optical parameters including the spatial frequency of projected fringes should be optimized according to the feature of the observed object and the measuring conditions. The intensity and contrast of the projected fringes are related to the output power of the laser beam and the background illumination, while the possibly higher output power of the laser beam might be necessary when the background illuminance is higher. The contrast of the generated sinusoidal fringe pattern using the developed optical system is about 100% in dark environment (i.e. the back ground illuminance $E = 0$). The decreased contrast caused by the background illumination and multiple scattering of the background medium will affect the measurement and the reconstruction, which is the main reason that we employ the narrow-band optical filter and polarizer to eliminate the noised signal contributed by the background illumination and multiple scattering. The spatial frequency of the projected fringe pattern is an important parameter for obtaining accurate reconstruction of the object being observed. The spatial frequency used in Figs. 4 and 6 are $1.0\ lp/mm$ and $2.0\ lp/mm$, respectively, while this selection of spatial frequency is based on preliminary experimental analyses. Generally speaking, the higher the spatial frequency, the better the accuracy of the reconstruction. If we measure a commercial coin using the developed method, the spatial frequency of $7\sim8$ lp/mm will yield the best accuracy.

We need to emphasize the coherence of the projected CW laser-beam-based signal generated by the designed optical system. The propagating optical signal keeps being coherent until reaching the observed object in the rain, which ensures that the high-contrast sinusoidal fringe patterns can be obtained at any position in the measuring rainy region without defocusing issue.

We should also point out that the artificial rain condition generated and employed in our investigation may differ from the natural rainy condition. Actually the attenuation coefficients that we measured for different rainfall values of the artificial rain condition had approximately agreed with the published data [40], [41], which might suggest that our method for generating the artificial rain condition was reasonable and useful based on the analysis in part C of Section II above.

V. Conclusion

With detailed theoretical analyses, mathematical derivations, and experimental results completed in this study, we have demonstrated that reliable measurements and accurate reconstructions can be obtained for determining 3D surface shapes of observed objects in the rain based on the combination of laser-beam-based sinusoidal fringe projection, the polarization technique, the optical filtering technique, and the Fourier-transform-based algorithm of reconstruction. The optical filtering technique has to be employed if the background illumination exists, while the effects resulted from the spectral absorption and multiple scattering on the propagation of the projected sinusoidal fringe pattern generated by the designed optical system in the rain can be mostly removed using the polarization technique. The application of the developed method does not suffer the limitation of focusing of the object being observed, precise synchronization, and the speed of measurement that might be a problem for the time-of-flight technique and digital-light-processing-based profilometry. The experimental results indicate the ability of the proposed method for accurately measuring a dynamic human face and a color object with varying reflectivity in the rain, even there exist the background illumination, the multiply-scattered light, the vibration from environmental influences including the wind, and the inhomogeneous medium of rain. The coherence of the projected CW laser-beam-based

signal generated by the designed optical system has been mathematically analyzed, which tells that the propagating optical signal keeps being coherent until reaching the observed object in the rain. It should be pointed out that the necessary high-contrast sinusoidal fringe patterns can be obtained at any position in the measuring rainy region without defocusing issue. The expected applications of the developed method and result of this work may include accurate in-situ shape determination of any 3D observed objects under rainy conditions and related target recognition including human face identification.

REFERENCES

[1] S. Van der Jeught and J. J. J. Dirckx, "Real-time structured light profilometry: A review," *Opt. Lasers Eng.*, vol. 87, pp. 18–31, 2016.

[2] S. Zhang, "High-speed 3D shape measurement with structured light methods: A review," *Opt. Lasers Eng.*, vol. 106, pp. 119–131, 2018.

[3] Z. Wang, "Review of real-time three-dimensional shape measurement techniques," *Measurement*, vol. 156, 2020, Art. no. 107624.

[4] N. Lazaros, G. C. Sirakoulis, and A. Gasteratos, "Review of stereo vision algorithms: From software to hardware," *Int. J. Optomechatronics*, vol. 2, no. 4, pp. 435–462, 2008.

[5] B. Tippetts, D. J. Lee, K. Lillywhite, and J. Archibald, "Review of stereo vision algorithms and their suitability for resource-limited systems," *J. Real-Time Image Process.*, vol. 11, pp. 5–25, 2016.

[6] S. Rusinkiewicz, O. Hall-Holt, and M. Levoy, "Real-time 3D model acquisition," *ACM Trans. Graph.*, vol. 21, pp. 438–446, 2002.

[7] M. Takeda and K. Mutoh, "Fourier transform profilometry for the automatic measurement of 3-D object shapes," *Appl. Opt.*, vol. 22, no. 24, pp. 3977–3982, 1983.

[8] Y. Wang and S. Zhang, "Superfast multifrequency phase-shifting technique with optimal pulse width modulation," *Opt. Exp.*, vol. 19, no. 6, pp. 5149–5155, 2011.

[9] S. Lei and S. Zhang, "Flexible 3-D shape measurement using projector defocusing," *Opt. Lett.*, vol. 34, no. 20, pp. 3080–3082, 2009.

[10] B. Li and S. Zhang, "Microscopic structured light 3D profilometry: Binary defocusing technique vs sinusoidal fringe projection," *Opt. Lasers Eng.*, vol. 96, pp. 117–123, 2017.

[11] P. Jia, J. Kofman, and C. English, "Two-step triangular-pattern phase-shifting method for three-dimensional object-shape measurement," *Opt. Eng.*, vol. 46, no. 8, 2007, Art. no. 083201.

[12] P. S. Huang, S. Zhang, and F.-P. Chiang, "Trapezoidal phase-shifting method for three-dimensional shape measurement," *Opt. Eng.*, vol. 44, no. 12, 2005, Art. no. 123601.

[13] J. Pan, P. S. Huang, and F.-P. Chiang, "Color phase-shifting technique for three-dimensional shape measurement," *Opt. Eng.*, vol. 45, no. 1, 2006, Art. no. 013602.

[14] S. Lei and S. Zhang, "Digital sinusoidal fringe pattern generation: Defocusing binary patterns VS focusing sinusoidal patterns," *Opt. Lasers Eng.*, vol. 48, no. 5, pp. 561–569, 2010.

[15] Y. Shuang and Z. Wang, "Active stereo vision three-dimensional reconstruction by RGB dot pattern projection and ray intersection," *Measurement*, vol. 167, 2020, Art. no. 108195.

[16] Y. Li and Z. Wang, "RGB line pattern-based stereo vision matching for single-shot 3-D measurement," *IEEE Trans. Instrum. Meas.*, vol. 70, 2021, Art. no. 5004413.

[17] Y. Li and Z. Wang, "3D reconstruction with single-shot structured light RGB line pattern," *Sensors*, vol. 21, no. 14, 2021, Art. no. 4819.

[18] U. Buck, S. Naether, B. Räss, C. Jackowski, and M. J. Tahli, "Accident or homicide–virtual crime scene reconstruction using 3D methods," *Forensic Sci. Int.*, vol. 225, no. 1-3, pp. 75–84, 2013.

[19] A. Marcin, S. Maciej, S. Robert, and W. Adam, "Hierarchical, three-dimensional measurement system for crime scene scanning," *J. Forensic Sci.*, vol. 62, no. 4, pp. 889–899, 2017.

[20] N. Yastikli, "Documentation of cultural heritage using digital photogrammetry and laser scanning," *J. Cultural Heritage*, vol. 8, no. 4, pp. 423–427, 2007.

[21] R. Zlot, M. Bosse, K. Greenop, Z. Jarzab, E. Juckes, and J. Roberts, "Efficiently capturing large, complex cultural heritage sites with a handheld mobile 3D laser mapping system," *J. Cultural Heritage*, vol. 15, no. 6, pp. 670–678, 2014.

[22] F. Yuan, D. Song, and L. Zeng, "Measuring 3D profile and position of a moving object in large measurement range by using tracking fringe pattern," *Opt. Commun.*, vol. 196, no. 1–6, pp. 85–91, 2001.

[23] P. J. Cobelli, A. Maurel, V. Pagneux, and P. Petitjeans, "Global measurement of water waves by Fourier transform profilometry," *Experiments Fluids*, vol. 46, pp. 1037–1047, 2009.

[24] B. Chen *et al.*, "Indoor and outdoor surface measurement of 3D objects under different background illuminations and wind conditions using laser-beam-based sinusoidal fringe projections," *Photonics*, vol. 8, 2021, Art. no. 178.

[25] M. Hnewa and H. Radha, "Object detection under rainy conditions for autonomous vehicles: A review of state-of-the-art and emerging techniques," *IEEE Signal Process. Mag.*, vol. 38, no. 1, pp. 53–67, Jan. 2021.

[26] D. Kijima *et al.*, "Time-of-flight imaging in fog using multiple time-gated exposures," *Opt. Exp.*, vol. 29, no. 5, pp. 6453–6467, 2021.

[27] T. Shi, Y. Qi, C. Zhu, Y. Tang, and B. Wu, "Three-dimensional microscopic image reconstruction based on structured light illumination," *Sensors*, vol. 21, no. 18, 2021, Art. no. 6097.

[28] W. S. Pegau, D. Gray, and J. R. V. Zaneveld, "Absorption and attenuation of visible and near-infrared light in water: Dependence on temperature and salinity," *Appl. Opt.*, vol. 36, no. 24, pp. 6035–6046, 1997.

[29] R. A. J. Litjens, T. I. Quickenden, and C. G. Freeman, "Visible and near-ultraviolet absorption spectrum of liquid water," *Appl. Opt.*, vol. 38, no. 7, pp. 1216–1223, 1999.

[30] D. J. Segelstein, "The complex refractive index of water," M. S. dissertation, Univ. of Missouri, Kansas City, 1981.

[31] L. R. Bissonnette, "Imaging through fog and rain," *Opt. Eng.*, vol. 31, no. 5, pp. 1045–1052, 1992.

[32] D. B. Lindell and G. Wetzstein, "Three-dimensional imaging through scattering media based on confocal diffuse tomography," *Nature Commun.*, vol. 11, 2020, Art. no. 4517.

[33] M. Grabner and V. Kvicera, "Multiple scattering in rain and fog on free-space optical links," *J. Lightw. Technol.*, vol. 32, no. 3, pp. 513–520, 2014.

[34] P. Singh and M. L. Singh, "Experimental determination and comparison of rain attenuation in free space optic link operating at 532 nm and 655 nm wavelength," *Optik*, vol. 125, no. 17, pp. 4599–4602, 2014.

[35] J. Guo, H. Zhang, and X. Zhang, "Propagating characteristics of pulsed laser in rain," *Int. J. Antennas Propag.*, vol. 2015, 2015, Art. no. 292905.

[36] S. Mori and F. S. Marzano, "Microphysical characterization of free space optical link due to hydrometeor and fog effects," *Appl. Opt.*, vol. 54, no. 22, pp. 6787–6803, 2015.

[37] A. Ishimaru, *Wave Propagation and Scattering in Random Media*. New York, NY, USA: Academic, 1978.

[38] J. W. Goodman, *Introduction to Fourier Optics*, 2nd ed. New York, NY, USA: McGraw-Hill, 1996, ch. 3.

[39] B. Chen, J. J. Stamnes, A. J. Devaney, H. M. Pedersen, and K. Stamnes, "Two-dimensional optical diffraction tomography for objects embedded in a random medium," *Pure Appl. Opt.: J. Eur. Opt. Soc. Part A*, vol. 7, pp. 1181–1199, 1998.

[40] T. S. Chu and D. C. Hogg, "Effects of precipitation on propagation at 0.63, 3.5, and 10.6 microns," *Bell Syst. Tech. J.*, vol. 47, no. 5, pp. 723–759, 1968.

[41] J. Guo and X.-J. Zhao, "Attenuation characterization of 532 nm and 1064 nm laser propagating in rain," *Optik*, vol. 127, no. 20, pp. 9088–9094, 2016.

[42] A. Maurel, P. Cobelli, V. Pagneux, and P. Petitjeans, "Experimental and theoretical inspection of the phase-to-height relation in Fourier transform profilometry," *Appl. Opt.*, vol. 48, no. 2, pp. 380–392, 2009.

[43] E. Zappa and G. Busca, "Static and dynamic features of Fourier transform profilometry: A review," *Opt. Lasers Eng.*, vol. 50, no. 8, pp. 1140–1151, 2012.

[44] H. Yun, B. Li, and S. Zhang, "Pixel-by-pixel absolute three-dimensional shape measurement with Fourier transform profilometry," *Appl. Opt.*, vol. 56, no. 5, pp. 1472–1480, 2017.

[45] Z. Wang, Z. Zhang, N. Gao, Y. Xiao, F. Gao, and X. Jiang, "Single-shot 3D shape measurement of discontinuous objects based on a coaxial fringe projection system," *Appl. Opt.*, vol. 58, no. 5, pp. A169–A178, 2019.